Acta Mech
https://doi.org/10.1007/s00707-024-04208-2

ORIGINAL PAPER

Vladimir Filkin · **Yury Vetyukov** · **Florian Toth**

Analytical model of induction heating buckling of a beam

Received: 27 September 2024 / Revised: 27 November 2024 / Accepted: 18 December 2024

Abstract Induction heating is an important technology for many engineering applications. Its modelling and analysis are challenging because it is a multiphysics phenomenon coupling geometrically nonlinear mechanics, electromagnetics and heat conduction. One of the challenges is buckling of thin plates and beams due to high temperatures and thermal gradients. The mechanical buckling changes the electromagnetic configuration of the model, thus changing the thermal solution, which affects mechanics back leading to a fully coupled problem. While this phenomenon has been studied numerically in the literature, it lacks an analytical treatment. We propose a closed-form analytical solution for the post-buckling deformation of induction heated beams. Using the solution, we conduct multiple parameter studies, aiming to gain a foundational understanding of the behaviour exhibited by the coupled system.

1 Introduction

Induction heating finds extensive application across diverse industries, owing to its capacity for rapidly and efficiently increasing temperatures directly within the target material. This feature makes it particularly valuable for numerous production processes, including material treatment and heating of transport belts during manufacturing operations [1]. Thin materials such as metal sheets, belts, electronic components and medical tubing benefit significantly from this heating method. Industries such as aerospace, semiconductor manufacturing and food production leverage its efficiency for various production needs illustrated in [2–4].

Significant temperature changes lead to thermal deformations, which cannot be omitted in the analysis because of their impact on the model configuration. Such thermal deformations are particularly of interest for thin structures, as they are prone to thermal buckling under high temperatures and high thermal gradients. Buckling introduces high deflections, thus changing the electromagnetic configuration and the temperature distribution, which in turn affects the post-buckling behaviour of the structure changing the equilibrium state of the whole system. Research works show the significance of the effect of thermal buckling on the induction heating process for various cases [5,6]. It is especially important for non-symmetric induction system layouts, for example, for the transverse one-sided inductor layout, which is used in various industrial applications shown in [3,5–8].

Numerical simulations allow us to study the influence of this phenomenon with high accuracy. Coupled finite element method (FEM) modelling procedures are presented for different applications [6,7,9,10]. Typically, the FEM approach consists of iterative subsequent solutions of electromagnetic, heat conduction and mechanical models with geometry and parameter update. It is designed to converge to the equilibrium state of the whole system for the given electric input. As a first step, the electromagnetic eddy current problem is solved for the non-deformed configuration. This provides a heat source to solve the heat conduction problem. Then, the

---

V.Filkin (✉)· Y.Vetyukov · F.Toth
Institute of Mechanics and Mechatronics, TU Wien, Getreidemarkt 9, 1060 Vienna, Austria
E-mail: vladimir.filkin@tuwien.ac.at

thermal strain is calculated and transferred to the nonlinear mechanical model. The next step is the transfer of the displacements from the mechanical model to electromagnetic and heat conduction models to update their mesh accordingly. Finally, the cycle repeats until a convergence criterion is satisfied. This method uses the concept of fixed point iteration, allowing us to analyse predetermined models, such as those used in industrial settings. However, it comes with several drawbacks: it demands significant computational resources, poses challenges in model construction due to intricate meshing and data transfer needs, and lacks the ability to explore the impact of all parameters on the system. As a result, this approach falls short of providing a comprehensive understanding of induction heating buckling from a fundamental standpoint.

Our goal is to investigate the complicated phenomena, relevant to practical applications on the basis of a novel simplified elasto-thermo-electromagnetic model problem, that reflects the principal coupling effects and demonstrates post-buckling behaviour as the real-world structures do. In the present contribution, we develop a comprehensive analytical solution for this model problem, which offers valuable insights into coupled system critical behaviour. The analytical approach allows for a deeper understanding of the interplay between the induction heating and the post-buckling behaviour of the beam, contributing to a more efficient and informed design methodology.

We use methods from various fields to develop an analytical solution for the coupled problem. For the electromagnetic model, we use coupled magnetic and electric circuit models. The heat conduction model requires a steady state energy balance. We elaborate on the mechanical model based on the nonlinear beam equation and Galerkin's and asymptotic approaches. The final relations for the coupled system are solved analytically with the assistance of the Wolfram Mathematica[1] computer algebra system.

2 Overview of the electro-thermo-mechanical model

We investigate a simplified test model of an induction heating process. The model is symmetric as illustrated in Fig. 1. The system layout is equivalent to a transformer with an air gap in the core, where the size of the air gap is governed by the mechanics of a flexible beam fixed at both ends. The magnetic core housing the input coil is positioned directly above the midpoint of the beam. The primary function of the second coil is to receive the energy from the electromagnetic system, heating the beam.

As the focus of the model is on an analytical investigation of the interconnectivity of physical phenomena governing the induction heating process, there is a difference between the proposed simplified model and the induction heating applications presented in [6,7,9,10]. Firstly, we have an electrically non-conductive beam; thus, the heating process is governed exclusively by the second coil. Secondly, the mechanical part is simplified to a clamped–clamped beam. Finally, the magnetic core is introduced to be able to use a network model for the electromagnetic system, which, however, is common in numerous real-world applications [11].

We impose an alternating voltage V_1 to the input coil, generating the alternating current I_1. The input coil creates an alternating magnetic field. It passes through the core and the air gap. The alternating magnetic field induces an electric current I_2 in the second coil. Then, the ohmic losses in the second coil heat the beam. Due to thermal expansion and the inability to expand freely, compressive stresses occur in the beam. At a critical temperature, the straight configuration of the beam becomes unstable and the beam buckles. The arising deflections change the air gap width. This changes the electromagnetic configuration and the total energy transferred to the system, which in turn affects the post-buckling behaviour.

In the following, we treat a coupled multiphysics problem involving electromagnetics, heat conduction and mechanics. To describe the buckling caused by induction heating, we need to build a relation between the deflections of the structure and the electrical input. For our model, deflections of the beam affect the air gap width. Thus, the first step is to derive the relations connecting the output current in the second coil with the input current and the gap width. Then we solve the thermal problem connecting the output current and the beam's temperature. Finally, we complete the coupled system by building a temperature–deflection relation.

3 Induction heating

We derive an analytical model describing the induction heating process. For this purpose, we combine electromagnetic and heat transfer models. Our objectives are to solve the system to obtain the relations for currents I_1 and I_2 and voltage in the output circuit V_2 for an imposed harmonic voltage V_1, and to calculate the final

---

[1] https://www.wolfram.com/mathematica/

temperature field of the beam. The resolved electrical circuits allow us to calculate the total input and output energies of the system and its efficiency in dependence on the size of the air gap.

3.1 Electromagnetic model

To solve the electromagnetic problem analytically, we need to use a number of assumptions. Firstly, we neglect the skin effect, no matter the input frequency. Secondly, we assume the flux is going through the magnetic core and the gap only; we neglect any stray fluxes, particularly the stray flux in the gap. Additionally, we assume a single turn in the input and output coils for simplicity.

The analytical solution for this example is based on the electromagnetic induction. The magnetic flux in the circuit can be calculated by the equation derived from Ampere's law (e.g. [12])

$$\Phi = L(I_1 - I_2), \tag{1}$$

where Φ (in Wb) denotes the total magnetic flux through the core, L (in H) is the inductance, and I_1 and I_2 (in A) represent the currents in input and output circuits, respectively. We use Faraday's law

$$V_{\mathrm{emf}} = -\frac{\mathrm{d}\Phi}{\mathrm{d}t}, \tag{2}$$

where V_{emf} (in V) denotes the electromotive force, Kirchhoff's voltage law (KVL) for the input and output circuits

$$V_1 = V_{R_1} + V_{\mathrm{emf}}, \quad V_2 = V_{R_2} = V_{\mathrm{emf}}, \tag{3}$$

and Ohm's law for the voltage over a resistor

$$V_{R_i} = R_i I_i. \tag{4}$$

Here R_i (in Ω) denotes a resistance, and V_k (in V) refers to a voltage.

We insert the flux equation (1) in Faraday's law (2). Additionally, applying the output KVL (3) and Ohm's law (4) leads to $V_{\mathrm{emf}} = R_2 I_2$. Thus, we obtain

$$R_2 I_2 = -L\left(\frac{\mathrm{d}I_1}{\mathrm{d}t} - \frac{\mathrm{d}I_2}{\mathrm{d}t}\right). \tag{5}$$

Then, we use Ohm's law and substitute the input KVL equation (3) and the previously obtained $V_{\mathrm{emf}} = R_2 I_2$ yielding

$$I_1 = \frac{V_{R_1}}{R_1} = \frac{V_1 - R_2 I_2}{R_1}. \tag{6}$$

Finally, we insert Eq. (6) into Eq. (5) and get the differential equation for the output current in the time domain

$$L\left(1 + \frac{R_2}{R_1}\right)\frac{\mathrm{d}I_2}{\mathrm{d}t} - R_2 I_2 = \frac{L}{R_1}\frac{\mathrm{d}V_1}{\mathrm{d}t}. \tag{7}$$

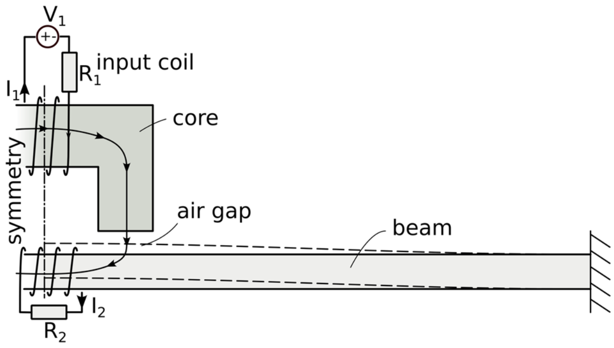

Fig. 1 Scheme of physics underlying the model

We switch to the frequency domain by assuming a harmonic input voltage $V_1 = \mathrm{Re}(\hat{V}_1 e^{j\omega t})$ and using an equivalent Ansatz for I_2, to obtain the algebraic equation

$$Lj\omega\left(1+\frac{R_2}{R_1}\right)\hat{I}_2 - R_2\hat{I}_2 = \frac{Lj\omega}{R_1}\hat{V}_1, \tag{8}$$

where $\hat{()}$ defines a complex amplitude. Solving it with respect to $\hat{I}_2$, we get

$$\hat{I}_2 = \frac{j\omega L\hat{V}_1}{j\omega L(R_1+R_2) - R_1R_2}. \tag{9}$$

The output voltage can be obtained with Ohm's law (4), and the current in the input circuit can be obtained from the frequency domain form of Eq. (6). The inductance is $L = \frac{1}{\mathcal{R}_\mathrm{M}}$. The magnetic reluctance $\mathcal{R}_M$ (in H^{-1}) consists of two parts: constant $\mathcal{R}_0$ (core and initial air gap) and changing $\mathcal{R}_w$ depending on the deflections of the beam

$$L = \frac{1}{\mathcal{R}_\mathrm{M}}, \quad \mathcal{R}_\mathrm{M} = \mathcal{R}_0 - \mathcal{R}_w = \mathcal{R}_0 - \frac{w}{\mu_\mathrm{gap}A_\mathrm{gap}}, \tag{10}$$

where w (in m) denotes the deflection in the middle of the beam, μ_gap (in H/m) stands for magnetic permeability of the gap and A_gap (in m^2) is the gap cross-sectional area (normal to the magnetic flux) of the gap (Fig. 1). If the beam deflects towards the core (positive deflections w), the air gap shrinks, causing the total magnetic reluctance $\mathcal{R}_\mathrm{M}$ to decrease. One has different approaches to define A_gap, for example, including fringing effects as in [13]. For the sake of simplicity, we assume $A_\mathrm{gap} = A_\mathrm{core}$, where A_core is the constant cross section of the magnetic core.

We aim to plot the efficiency characteristics of the electromagnetic system depending on its parameters. The electrical efficiency can be calculated as follows

$$\eta_\mathrm{eff} = \frac{\mathrm{Re}(S_2)}{\mathrm{Re}(S_1)}, \tag{11}$$

where S_1 and S_2 (in VA) are input and output complex powers. A complex power S_i is calculated by Eq. (12). We multiply a complex voltage and a complex conjugate of a complex current

$$S_i = \frac{\hat{V}_i\overline{\hat{I}_i}}{2}, \tag{12}$$

where $\overline{()}$ denotes a complex conjugate. We use the non-dimensional frequency and resistance parameters

$$\tilde{\omega}_\mu = \frac{\omega}{R_2\mathcal{R}_M}, \quad \tilde{R} = \frac{R_1}{R_2}, \tag{13}$$

to plot the electric efficiency of the system in Fig. 2. The figure shows a high-efficiency plateau for high $\tilde{\omega}_\mu$ and $\tilde{R}$. Efficiency drops to zero at low frequency and resistance parameters. It remains constant for the low resistance parameter across a wide range of $\tilde{\omega}_\mu$.

In a typical induction heating system [14], the operating frequency ω ranges from a few kHz to several MHz. The electrical resistivity of materials used is usually between 10^{-7} and 10^{-8} Ωm, while the magnetic permeability ranges from 10^{-2} to 10^{-6} H/m. These properties result in values of $\tilde{\omega}_\mu$ greater than 1. However, $\tilde{\omega}_\mu$ is often limited due to the skin effect, which is undesirable in many scenarios, such as when uniform through-thickness heating is required. The parameter $\tilde{R}$ typically exceeds 1, as this improves the efficiency of the induction system.

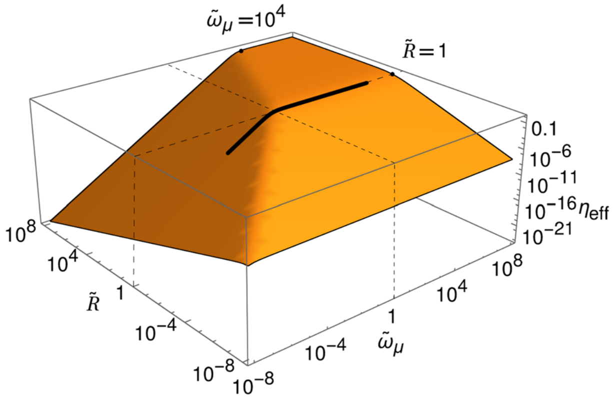

Fig. 2 Efficiency study for the electromagnetic system. The x- and y-axes stand for the non-dimensional parameters $\tilde{\omega}_\mu$ and $\tilde{R}$. The z-axis represents the efficiency of the system. All the axes are in logarithmic scale. The thick black line represents the loading range from Fig. 6

3.2 Heat transfer

With the thermal model, we connect the electric energy dissipated in the output resistor with the temperature of the beam. We assume a steady state, only one heat source due to the period-averaged Ohmic losses from induction heating, and cooling due to the surrounding air. Additionally, a high thermal conductivity of the beam is assumed, so the heat generated by the induction is uniformly distributed over the beam. This leads to a spatially constant temperature. Thus, the beam temperature can be obtained directly from the balance of energy

$$\operatorname{Re}(S_2) = Q_{\text{air}}, \text{ or } \frac{I^2 R_2}{2} = h A_{\text{T}}(T - T_0), \tag{14}$$

where $\operatorname{Re}(S_2)$ (in W) is the real part of the induction heating complex power, Q_{air} (in W) denotes the cooling power, $I = ||\hat{I}_2||$ from Eq. (9), T (in K) is the temperature of the beam, T_0 denotes the temperature of the air, A_{T} (in m^2) is the area of the beam in contact with the air and h (in W/m^{2}K) is the heat transfer coefficient. From Eq. (14), we get the current–temperature relation

$$T = \frac{I^2 R_2}{2 h A_{\text{T}}} + T_0. \tag{15}$$

For simplicity, we set $T_0 = 0$ for further calculations. We also decoupled A_{T} from the mechanical dimensions of the beam to study different effects separately.

4 Thermal post-buckling

We aim to derive an approximation of the beam deflection for supercritical temperatures. As the beam is fixed on both ends and the temperature is uniform, we have a constant distribution of the compression force over the beam (Fig. 3). Here we define the force $P = P_{\text{crit}} + \Delta P$ (in N), where P_{crit} is Euler critical load and ΔP represents the difference between the actual force and the critical force value at which the buckling is initiated. Thus, firstly, we define the dependence of deflection on ΔP. Then, we build a relation between the temperature and ΔP to get the post-buckling relation for the thermal loading.

4.1 Force–deflection relation

The first critical load and the associated buckling mode shape are known from Euler's linear beam buckling theory, see e.g. [15]. For our case (beam clamped on both sides), we have

$$w(s) = w_0(-1 + \cos(k_l s)), \quad k_l = \frac{2\pi}{l}, \quad P_{\text{crit}} = \frac{4\pi^2 E J}{l^2}, \tag{16}$$

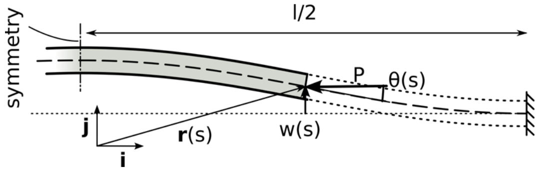

Fig. 3 Mechanical model with kinematics. The applied force $P = P_{\text{crit}} + \Delta P$

where $w(s)$ (in m) denotes the deflections of the beam, w_0 is the unknown deflection amplitude parameter, s in $[0, l]$ (in m) is the material coordinate of the beam, l (in m) represents the length of the beam, E (in Pa) denotes Young's modulus and J (in m^4) represents the moment of inertia of the beam cross section.

Linear theory does not allow us to determine the unknown w_0 at the post-buckling stage. Therefore, we need to use a nonlinear theory, assuming that the relation for $w(s)$ from Eq. (16) holds for $P \geq P_{\text{crit}}$ as long as ΔP is small. The nonlinear beam equation is

$$EJ\theta''(s) + (P_{\text{crit}} + \Delta P)\sin(\theta(s)) = 0, \tag{17}$$

where $\theta(s)$ is an angle of the deformation (see Fig. 3) and the symbol $(\,)' = \frac{\partial(\,)}{\partial s}$ denotes the derivative with respect to the material coordinate s. At small deformations, the deflections and the angle are related by

$$\theta(s) = w'(s) = -w_0 k_l \sin(k_l s). \tag{18}$$

One can utilise various mathematical approaches to find the relation for the unknown kinematic variable w_0. We introduce two methods. One is based on Galerkin's procedure, which is known for this problem [16]. The other is developed based on the asymptotic approach and requires no a priori assumptions as in Eq. (16).

First, we apply Galerkin's method. The method is used to approximate the solution of a differential equation. The main idea is to minimise the residual error by selecting a suitable basis function, which usually results in simple algebraic equations [17]. In our specific problem, we choose the expression for the angle of deformation (18) without $w_0 k_l$ as our basis function. We insert Eq. (18) into the beam equation (17). Then, we multiply the resulting relation by the basis function $\sin(k_l s)$ and integrate over the length. This reformulates our initial problem, aiming to minimise the residual error in the solution.

$$\int_0^l \sin(k_l s)\left[-w_0 k_l^3 \sin(k_l s) + \left(\frac{\pi^2}{4l^2} + \frac{\Delta P}{EJ}\right)\sin\left(w_0 k_l \sin(k_l s)\right)\right]\mathrm{d}s = 0. \tag{19}$$

Evaluating the integral, we arrive at the equation

$$J_1(w_0 k_l)\left(\frac{\Delta P l}{EJ} + k_l^2 l\right) - \pi k_l^2 w_0 = 0, \tag{20}$$

where $J_1(\,)$ is the Bessel function of the first kind. To obtain an approximate closed-form solution, we perform a series expansion of the Bessel function in Eq. (20) up to the third order with respect to w_0 and get

$$-\frac{w_0^3 \pi^3 \left(\frac{\Delta P l^2}{EJ} + 4\pi^2\right)}{2l^4} + \frac{w_0 \pi \Delta P}{EJ} = 0.$$

Solving the equation with respect to w_0 results in

$$w_{\text{G}} = 2w_0 = \frac{2\sqrt{2}l\sqrt{\Delta P}}{\pi\sqrt{\Delta P + \frac{4\pi^2 EJ}{l^2}}}, \tag{21}$$

where w_{G} denotes the deflection in the middle of the beam obtained with Galerkin's method.

Galerkin's method is an approximation-based method which does not guarantee the asymptotic accuracy of the solution. So, we additionally determine w_0 using the asymptotic method to verify Eq. (21). The method is utilised for deriving closed-form solutions, for example, in [18,19]. We add a small parameter λ into the beam equation (17), which indicates the smallness of ΔP:

$$EJ\theta''(s) + (P_{\text{crit}} + \lambda^2 \Delta P)\sin(\theta(s)) = 0. \tag{22}$$

Then, we represent the solution as a series expansion with respect to this small parameter guessing the first term based on the expression for the angle of the deformation Eq. (18)

$$\theta(s) = k_l w_0 \lambda \sin(k_l s) + \sum_{i=2}^{\infty} \lambda^i \theta_i(s) \tag{23}$$

where the correction terms θ_i are unknown functions. The power of λ in Eq. (22) corresponds to the known fact that the small deflections are proportional to the square root of ΔP, established by numerical solutions of the nonlinear beam equations.

We substitute Eq. (23) to the modified beam equation Eq. (22) and collect coefficients at different powers of the small parameter λ^i, which produces an infinite system of equations. These equations can be solved independently, and the solutions should satisfy the homogeneous BCs of the original problem. The equations for the first two terms ($i = 1, 2$) are satisfied identically. The third equation for λ^3 is

$$\theta_3''(s) + k_l^2 \theta_3(s) = k_l w_0 \sin(k_l s) \left(\frac{1}{6} k_l^4 w_0^2 \sin^2(k_l s) + \frac{\Delta P}{EJ} \right). \tag{24}$$

The minor correction term θ_3 itself has no importance. However, the equation (24) contains our unknown w_0 and should satisfy the boundary conditions of the original problem, i.e. $\theta_3(0) = 0$ and $\theta_3(l) = 0$. The inhomogeneous boundary value problem is only solvable when the right-hand side contains no first harmonic and thus orthogonal to $\sin(k_l s)$. Indeed, by multiplying the left-hand side of Eq. (24) with $\sin(k_l s)$, integrating over the length, using integration by parts and taking the boundary conditions into account, we obtain

$$\int_0^l (\theta_3''(s) + k_l^2 \theta_3(s)) \sin(k_l s) \mathrm{d}s = 0. \tag{25}$$

Now, we are in the position to determine w_0. Multiplying the right-hand side of Eq. (24) by $\sin(k_l s)$, integrating from 0 to l and equating the integral to zero, we obtain an equation for w_0, which results in the expression

$$w_{\mathrm{A}} = 2 w_0 = \frac{\sqrt{2} l^2 \sqrt{\Delta P}}{\pi^2 \sqrt{EJ}}, \tag{26}$$

where w_{A} is the deflection in the middle of the beam obtained with the asymptotic method. The employed procedure is similar to the Poincaré–Lindstedt method, but uses the solvability instead of the periodicity condition [20].

The expression (26) resembles the results obtained from Galerkin's method Eq. (21). The difference is that the Galerkin's result has an additional term in the denominator depending on $\sqrt{\Delta P}$, which becomes equivalent to Eq. (26) after linearisation. We compare the results obtained by Galerkin and asymptotic methods with the numerical solution of the beam equation Eq. (17) in Fig. 4. The numerical solution is obtained using Wolfram Mathematica. We plot the non-dimensional deflections in the middle of the beam $\frac{w_0}{l}$ against the normalised supercritical force $\frac{\Delta P}{P_{\mathrm{crit}}}$.

As we can see from the graph, Galerkin's approximation matches the numerical solution with high accuracy: the relative error is less than 5% for up to 10% of additional load above critical. The asymptotic solution's deviation is almost two times higher at this force level. The accuracy can be further increased by solving the equation resulting from Galerkin's approach (20) with the Bessel function without series expansion or by including higher-order terms in the expansion in the asymptotic approach. As ΔP is small for all our numerical experiments and the main goal is to investigate the system behaviour qualitatively, we are not focusing on higher-accuracy models.

4.2 Temperature–deflection relation

The last step is to find the relation between T and ΔP for the system depicted in Fig. 3. To do this, we use the following geometrical relationships. First, we calculate the derivative of the position vector of the deformed configuration with respect to the material coordinate s, given as $\boldsymbol{r}'(s) = y'(s)\boldsymbol{j} + x'(s)\boldsymbol{i}$, yielding a local

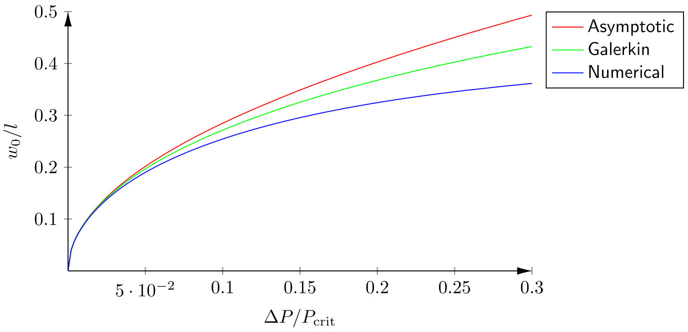

Fig. 4 Post-buckling deformation: comparison of Galerkin and asymptotic methods with the numerical solution. Only the positive branch of the bifurcation diagram is shown

direction vector. Since the distance between the supports l is given, we can relate it to the integral of the x-projection of the direction vector $\boldsymbol{r}'(s)$. We thus have

$$l = \int_0^l x'(s)\mathrm{d}s. \tag{27}$$

As shown in [21], the first derivative of x is related to the strains and the angle of deformation as

$$x'(s) = (1+\epsilon)\cos(\theta) \approx (1+\epsilon)\left(1 - \frac{1}{2}w'(s)^2\right). \tag{28}$$

Here ϵ is the axial strain, which is constant for our loading case and assumptions, and we keep just the quadratic terms of the power series concerning the transverse deflection. According to Hooke's law, the strains in the beam are defined by

$$\epsilon = \alpha T - \frac{P}{EA} = \alpha T - \frac{P_{\text{crit}}}{EA} - \frac{\Delta P}{EA}, \tag{29}$$

where A is the cross-sectional area of the beam. Here, we assume that the reference temperature for thermal expansion is zero. We insert Eq. (28) into the integral Eq. (27) to obtain

$$l = (1+\epsilon)\int_0^l \left(1 - \frac{1}{2}w'(s)^2\right)\mathrm{d}s. \tag{30}$$

Then we replace $w'(s)$ by the buckling mode for the deformation angle Eq. (18):

$$l = (1+\epsilon)\int_0^l \left(1 - \left(\frac{w_{\mathrm{G}}}{2}\frac{2\pi}{l}\sin\left(\frac{2\pi s}{l}\right)\right)^2\right)\mathrm{d}s. \tag{31}$$

Here we use Galerkin's approximation for the post-critical deflections for the beam w_{G}. After integration, one obtains

$$l = (1+\epsilon)\left(l - \frac{\pi^2 w_{\mathrm{G}}^2}{4l}\right). \tag{32}$$

We insert the equation for the strains (29) and the Galerkin's approximation (21) to the expression for the total length of the beam (32). Then we solve it for the post-critical load ΔP to obtain

$$\Delta P = \frac{1}{2l^4}\left(-EAl^4(-\alpha T - 2) - \sqrt{E^2A^2l^8(-\alpha T - 2)^2 - 4E^2Jl^4(4\pi^2 A\alpha l^2 T - 16\pi^4 J)}\right).$$

This can be inserted back into the Galerkin's approximation (21) yielding

$$w_{\mathrm{G}}(T) = \frac{2\sqrt{2}l}{\pi}\frac{\sqrt{EA(\alpha T + 2) - \frac{d}{l^4}}}{\sqrt{EA(\alpha T + 2) - \frac{d}{l^4} + \frac{8\pi^2 EJ}{l^2}}}, \tag{33}$$

with $d = \sqrt{E^2 l^4 \left(A^2 l^4 (\alpha T + 2)^2 + J(64\pi^4 J - 16\pi^2 A\alpha l^2 T)\right)}$. The derived equation directly relates temperature and deflection. An analogous computation could be done for the asymptotic method but is omitted due to the lower accuracy as demonstrated in Sect. 4.1.

5 Analysis of the coupled model

Having the closed-form solution derived for the induction heating and thermal post-buckling, we proceed with an analysis of the behaviour of the coupled model with energy input, displacements and temperature outputs. We introduce a set of non-dimensional parameters beginning with the electromagnetic quantities:

$$\tilde{\omega} = \frac{\omega}{R_2 \mathcal{R}_0}, \quad \tilde{R} = \frac{R_1}{R_2}, \tag{34}$$

non-dimensional frequency and non-dimensional resistance, respectively. The non-dimensional frequency parameter for the coupled system differs from the one of the electromagnetic system $\tilde{\omega}_\mu$ from Eq. (13). Now, we consider only the initial reluctance $\mathcal{R}_0$ from the designed gap width without taking buckling deflections into account. For the uncoupled electromagnetic system (Eq. (13)), we consider the total reluctance $\mathcal{R}_\mathrm{M}$. Then, we define the coupling parameter (non-dimensional reluctance) and the non-dimensional input power

$$\tilde{\mathcal{R}} = \frac{\frac{h}{\mu_\mathrm{gap} A_\mathrm{gap}}}{\mathcal{R}_0}, \quad \tilde{S} = \frac{\mathrm{Re}(S_1)}{S_\mathrm{crit}}, \tag{35}$$

respectively, where h is the thickness of the beam and S_crit is the input power required to achieve buckling instability. Finally, we require the output parameters, namely the non-dimensional displacement and the non-dimensional temperature

$$\tilde{w} = \frac{w_\mathrm{G}}{h}, \quad \tilde{T} = \frac{T}{T_\mathrm{crit}}, \tag{36}$$

respectively, where T_crit is the temperature corresponding to the Euler critical load P_crit.

The coupled system of equations consists of the temperature–deflection relation $w(T)$ (33) and the function of temperature over input voltage and deflections $T(\mathrm{Re}(\hat{V}_1), w)$ combining Eqs. (9), (10) and (15). Instead of the voltage, we use the input power, as every input voltage can be related to an input power. Since the functions $T(\mathrm{Re}(S_1), w)$ and $w(T)$ are bijective, we can build the closed-form solution using the following strategy: firstly, we define a temperature range in which we want to acquire the equilibrium state of the system. As deflections towards the inductor and away from it correspond to one temperature, we obtain two deflection values from the temperature–deflection relation (33) for each temperature. The deflections have equal amplitudes but opposite signs. We use Eq. (15) to determine the required output currents I for the given temperature. Then, we compute the inductance of the electromagnetic system with Eq. (10). We now have two inductances: one corresponding to buckling towards the inductor and the other to buckling away from it. As the last step, we obtain the input powers for corresponding computed inductances and the output current with Eq. (9).

5.1 Bifurcation diagrams

Knowing how to find the system's equilibrium, we plot the bifurcation displacement and temperature diagrams. We apply different temperatures up to 20% above the critical and obtain displacements and input energies. To show the influence of the non-dimensional parameters $\tilde{\omega}$, $\tilde{R}$ and $\tilde{\mathcal{R}}$, we conduct three experiments, varying one of the parameters and fixing the other two. The results for the non-dimensional displacement and temperature are presented in Fig. 5. Firstly, we vary the frequency parameter $\tilde{\omega} = 0.01, 1, 100$ with the fixed $\tilde{R} = 1$ and $\tilde{\mathcal{R}} = 1$ (Fig. 5 A). Then, we show the influence of the resistance parameter in Fig. 5 B for $\tilde{R} = 0.01, 1, 100$ and $\tilde{\omega} = 1$ and $\tilde{\mathcal{R}} = 1$. Finally, Fig. 5 C shows bifurcation diagrams for different coupling parameters $\tilde{\mathcal{R}} = 0.1, 1, 10$ and $\tilde{\omega} = 1$ and $\tilde{R} = 1$. The core reluctance is set to zero for simplicity, as it is negligibly small compared to the gap reluctance for most realistic core materials and gap widths. Thus, $\mathcal{R}_0$ includes only the initial gap reluctance.

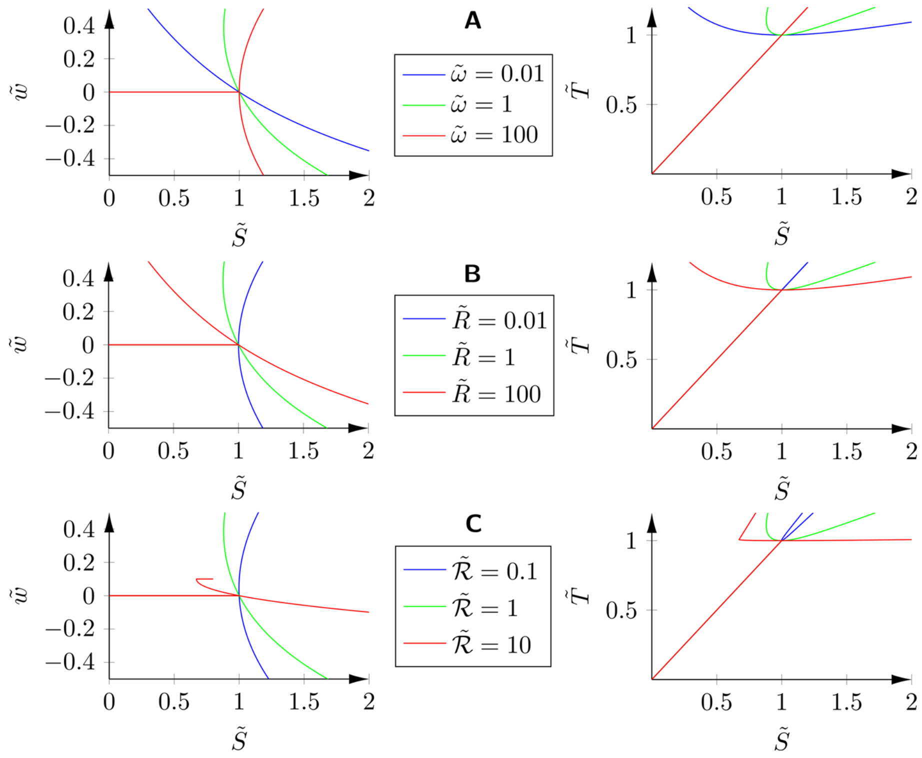

Fig. 5 Deflection bifurcation diagrams (left) and temperature bifurcation diagrams (right) for different non-dimensional parameters. The non-dimensional deflection $\tilde{w}$ and non-dimensional temperature $\tilde{T}$ are plotted over the non-dimensional input power $\tilde{S}$. The beam is heated up to $\tilde{T} = 1.2$. The trivial unstable solution is not shown. **A** We vary non-dimensional frequency $\tilde{\omega}$ and fix $\tilde{\mathcal{R}} = 1$ and $\tilde{R} = 1$. **B** We vary non-dimensional resistance $\tilde{R}$ and fix $\tilde{\omega} = 1$ and $\tilde{\mathcal{R}} = 1$. **C** we vary non-dimensional coupling $\tilde{\mathcal{R}}$ and fix $\tilde{\omega} = 1$ and $\tilde{R} = 1$

Bifurcation diagrams for induction heating-induced buckling differ from the standard thermal buckling diagrams. For various non-dimensional parameters, the branches of the graphs are angled or distorted in a non-symmetric way. This happens due to the change of the efficiency (see Fig. 2) in the system caused by the total reluctance shift. The upper branches of deflection bifurcation diagrams in Fig. 5 represent buckling towards the magnetic core and the inductor. If a beam buckles towards the magnetic core, the total magnetic reluctance of the system decreases, and the efficiency η_{eff} from Eq. (11) increases. This means the beam temperature is higher for the same input of the electromagnetic system. The minimum of the post-critical state electrical power S_{min} shifts from the bifurcation point to the branch depicting buckling towards the inductor. The meaning of S_{min} is further illustrated in Fig. 8 A and C. This can lead to "snap-through" behaviour of the beam, meaning that the beam would reach high deflection immediately at the critical power input.

On the other hand, if a beam buckles away from the magnetic core (lower branches of deflection bifurcation diagrams in Fig. 5), the total magnetic reluctance of the system increases, and the efficiency drops. Such a behaviour of the system makes the bifurcation diagram unsymmetric and transcritical [22]. The transcritical ("snap-through") effect grows with a high resistance parameter or low frequency parameter. On the other hand, with a low resistance parameter or high frequency parameter, the plot resembles the standard supercritical thermal buckling.

We observe a specific case of buckling towards the magnetic core in Fig. 5 C. In this scenario, the deflection of the beam reaches the initial gap width in the plot for $\tilde{\mathcal{R}} = 10$ when buckling towards the magnetic core. The beam rests against the magnetic core from $\tilde{w} = 0.1$ onward, creating a jump in the first derivative of the graph at this point. This behaviour is out of the scope of our mechanical model. However, we assume that for $\tilde{T}$ close to 1, the deflection $\tilde{w}$ does not change with increasing power input. Thus, no changes to the inductance (Eq. (10)) are introduced at higher temperatures. This assumption leads to the linear temperature–energy relation, since T no longer depends on the deflection (Eqs. (9) and (15)). The behaviour is evident in the right plot of Fig. 5 C for $\tilde{\mathcal{R}} = 10$ following the discontinuity in the first derivative.

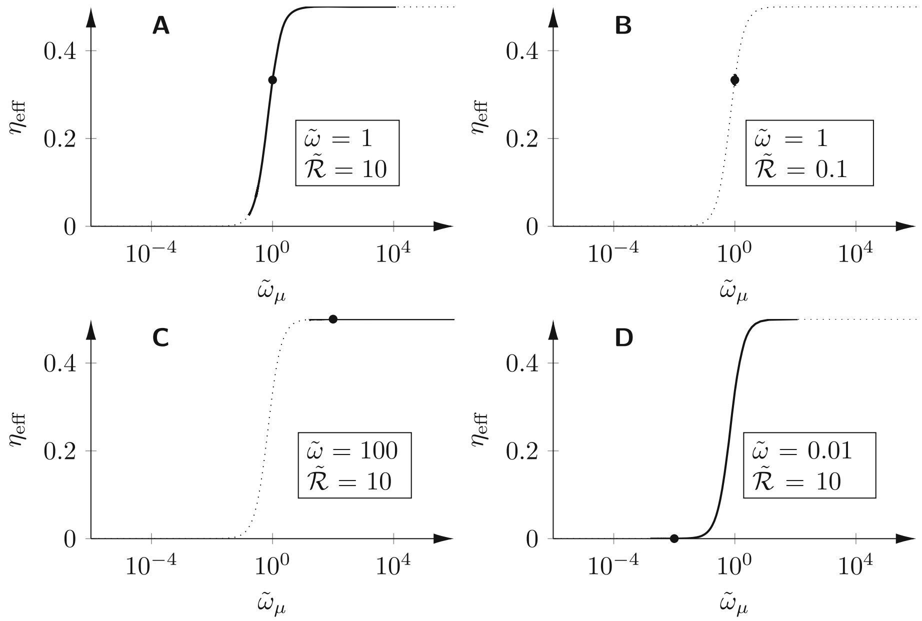

Fig. 6 The 2D slices of the electromagnetic system efficiency 3D diagram (dotted line) (see Fig. 2) with the loading paths (solid line) and the initial starting point (dot) are presented. The range of the loading paths is also depicted by a solid line in Fig. 2. The model is heated up to $T_{\text{crit}} = 1.2$. The system efficiency η_{eff} is plotted over the non-dimensional frequency $\tilde{\omega}_{\mu}$, including the total reluctance of the system. For all the graphs, $\tilde{R} = 1$. The initial parameters for the starting points are depicted in the boxes for each graph. **A** $\tilde{\omega} = 1$ and $\tilde{\mathcal{R}} = 10$. **B** $\tilde{\omega} = 1$ and $\tilde{\mathcal{R}} = 0.1$. **C** $\tilde{\omega} = 100$ and $\tilde{\mathcal{R}} = 10$. **D** $\tilde{\omega} = 0.01$ and $\tilde{\mathcal{R}} = 10$

The temperature bifurcation diagrams, shown in the right-hand plots of Fig. 5, follow the same pattern. In the absence of significant influence of the electromagnetic model on thermal buckling, one observes only linear temperature dependency on input energy ($\tilde{\omega} = 100$ of the right plot in Fig. 5 A or $\tilde{R} = 0.01$ of the right plot in Fig. 5 B). Opposite, we see an unsymmetric bifurcation at the critical temperature for the considerable influence of the electromagnetic system on the critical behaviour of the beam.

5.2 Coupling parameter

The influence of the coupling parameter (Fig. 5 C) differs significantly. To study it, we investigate its influence on the change in the efficiency of the electromagnetic system. We take 2D slices of the plot in Fig. 2 with different initial frequency and resistance parameters and the coupling parameter. The coupling parameters define the rate of the change. Initial frequency and resistance parameters define the initial point on the plot. We heat the system up to T_{crit} and plot the starting point, which represents the state of the system in the bifurcation point. Then we heat the system up to $1.2T_{\text{crit}}$ (as in Fig. 5). The buckled system follows one of two paths to the left or the right from the starting point, depending on whether the beam buckles towards or away from the coil. This is determined manually in our model but in practice is guided by the small initial imperfection. The paths represent the change in the non-dimensional frequency parameter, including the whole reluctance of the system Eq. (13). Thus, the non-dimensional frequency, which includes only the initial reluctance of the system $\mathcal{R}_0$, is the initial parameter for the actual non-dimensional frequency parameter, which takes the deformations into account. The results are presented in Fig. 6.

The coupling parameter defines the rate of change of the frequency parameter with respect to the beam's deflections. A high coupling parameter allows for significant change in the efficiency of the electromagnetic system due to the substantial impact of deflection changing the gap width. Thus, it affects the post-buckling behaviour of the beam by the unsymmetry of the two paths to the left and right from a starting point in Fig. 6 A and B. These figures correspond to plots for $\tilde{\mathcal{R}} = 10$ and 0.1 in Fig. 5 C.

The resistance and frequency parameters define the initial point in the plot (Fig. 6 C and D). Due to the non-symmetric behaviour of the system, we observe a significant influence of the initial point. In Fig. 6 C, there is almost no change in efficiency, even with a significant impact of deformations on system reluctance,

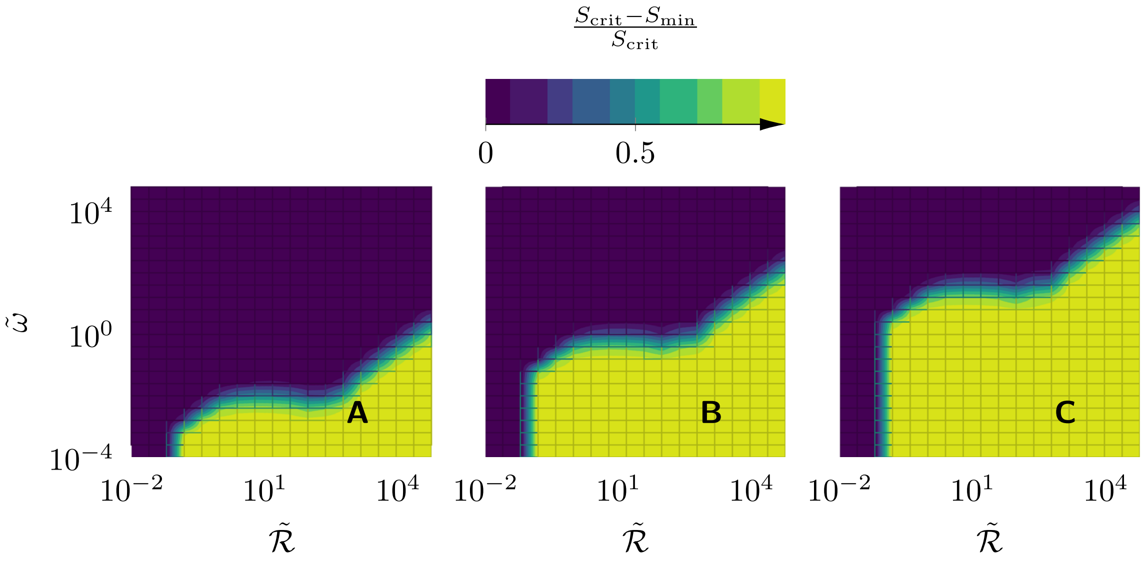

Fig. 7 Transcritical ("snap-through") effect analysis parameter space. The plots represents $\frac{S_{\mathrm{crit}}-S_{\mathrm{min}}}{S_{\mathrm{crit}}}$ over the frequency and coupling non-dimensional parameters. The x- and y-axes are on a logarithmic scale. Three plots correspond to three different non-dimensional resistances: **A** $\tilde{R} = 0.001$. **B** $\tilde{R} = 1$. **C** $\tilde{R} = 1000$

represented by a large coupling parameter. In Fig. 6 D, we have a dramatic change in the system's efficiency with the same impact as the deflections.

5.3 Transcritical behaviour

The next step is to analyse the transcritical effect of the bifurcation quantitatively. We define another non-dimensional parameter, the transcritical effect power measure

$$\frac{S_{\mathrm{crit}} - S_{\mathrm{min}}}{S_{\mathrm{crit}}},$$

where S_{min} denotes the minimum post-critical state electrical power (Fig. 8 A and C). Power S_{min} has no clear physical meaning for the system and serves as a characteristic of the obtained transcritical bifurcations. The transcritical effect power measure varies only from 0 to 1, where 0 is the case of pure thermal buckling. We plot the transcritical effect power measure parameter in 3D parameter space with respect to the coupling and frequency parameters. We also vary the resistance parameters $\tilde{R} = 0.001, 1, 1000$ to show its impact on the plot. We obtain three plots corresponding to different $\tilde{R}$ presented in Fig. 7. The coupling and frequency parameters are depicted on a logarithmic scale, while the transcritical effect parameter is presented on a linear scale to clearly distinguish between high and low transcritical unsymmetric effects.

The "snap-through" effect of the system for buckling towards the magnetic core intensifies for lower frequency and higher coupling parameters. We observe the significantly lower transcritical effect when the coupling parameters are below 10^{-1}. From the comparison of the three figures, it is apparent that the resistance parameter shifts the border between transcritical unsymmetric and symmetric systems in $\tilde{\omega}$-direction. Specifically, higher values of $\tilde{R}$ result in transcritical effect persisting at higher values of $\tilde{\omega}$.

As the next step, we show the effect's practical importance by introducing the beam's initial imperfection. We modify the nonlinear beam equation (17) with the new undeformed configuration, resembling the buckling shape Eq. (18)

$$EJ\left(\theta''(s) - A_0 k_l^2 \sin(k_l s)\right) + (P_{\mathrm{crit}} + \Delta P)\sin(\theta(s)) = 0, \tag{37}$$

where A_0 is an amplitude parameter of the initial imperfection in the form of the buckling mode. Following the same procedure as for the ideal case (Eq. (17)), we relate the deflection and temperature of the beam thermal buckling and use it within the established setup for the coupled model. Our goal lies in demonstrating the

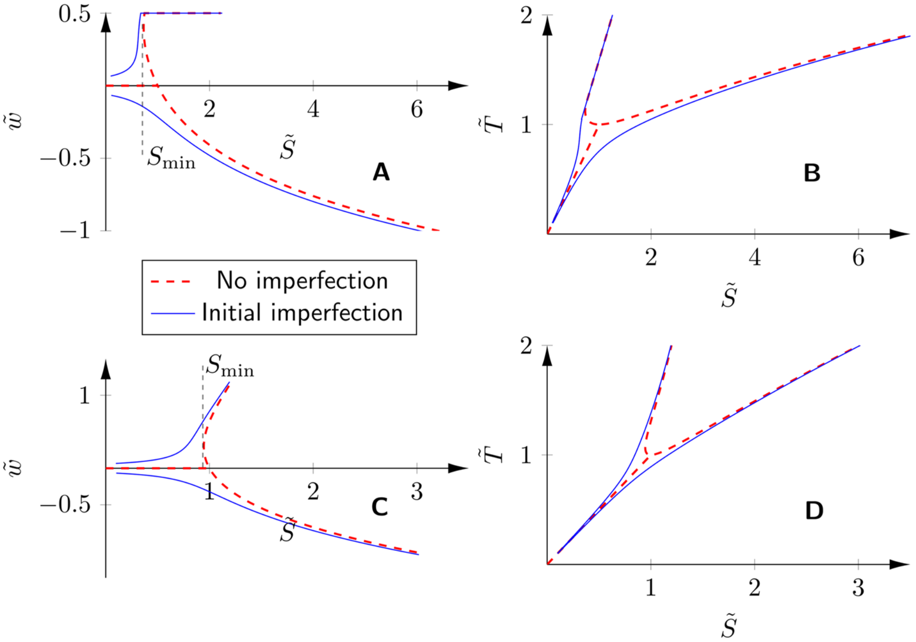

Fig. 8 Deflections (**A**, **C**) and temperature (**B**, **D**) bifurcation diagrams for two cases—with initial imperfection and without it. The system parameters are $\tilde{\omega} = 1$, $\tilde{R} = 1$ and $A_0 = 0.01hk_l$. For figures **A** and **B**, $\tilde{\mathcal{R}} = 5$. For figures **C** and **D**, $\tilde{\mathcal{R}} = 0.5$

arising effects and their importance for the system, not in quantifying the initial imperfection impact on the system's behaviour. Thus, we plot the bifurcation diagram for the temperatures up to $2T_{\text{crit}}$ for the mechanical system with and without initial imperfection. For this experiment, we choose $\tilde{\omega} = 1$, $\tilde{R} = 1$, $\tilde{\mathcal{R}} = 5$ and $A_0 = 0.01hk_l$.

Figure 8 shows that the actual critical energy and temperature drop when the beam buckles towards the magnetic core in the presence of an initial imperfection. The reduction of the critical energy depends on the sharpness of the unstable brunch and the initial imperfection parameter A_0. Comparing Fig. 8 A and C supports this conclusion, showing that non-dimensional parameters influence the reduction of critical energy. For absolutely unstable cases, when the transcritical effect energy measure equals 1 (Fig. 7), we expect an instant jump in the deflection for significantly high A_0. Furthermore, from the coupled system with an initial imperfection, we observe that only the sign of the initial imperfection defines the bifurcation branch for the whole system.

6 Conclusion

As induction heating modelling, including buckling effects, lacks thorough analytical analysis, we proposed a test system and developed its coupled analytical model. The obtained results clearly showed the importance of the coupling effect both on the post-critical behaviour of the beam and on the efficiency of the induction heating. The unsymmetry of the bifurcation diagrams results from the coupling and their transcritical development depends on the introduced parameters. We investigated the influence of frequency, reluctance and resistance non-dimensional parameters on the transcritical behaviour of the system. Arising transcritical effect of the post-buckling state may cause significant changes in the induction heating process, as one can observe the "snap-through" effect if the beam buckles towards the core.

Funding Open access funding provided by TU Wien (TUW). This research was funded by the Austrian Research Promotion Agency (FFG) under the BRIDGE program, project Induction-Buckling (project number FO999903663). The authors acknowledge TU Wien Bibliothek for financial support through its Open Access Funding Programme.

Declarations

Conflict of interests The authors have no relevant financial or non-financial interests to disclose.

References

1. Lucia, O., Maussion, P., Dede, E.J., Burdio, J.M.: Induction heating technology and its applications: Past developments, current technology, and future challenges. IEEE Trans. Industr. Electron. **61**, 2509–2520 (2014). https://doi.org/10.1109/TIE.2013.2281162
2. Lozinskiĭ, M.G.: Industrial Applications of Induction Heating. Pergamon Press, Oxford (1969)
3. El-Mashad, H.M., Pan, Z.: Application of induction heating in food processing and cooking. Food Eng. Rev. **9**, 82–90 (2017). https://doi.org/10.1007/S12393-016-9156-0
4. Zhang, T., Li, D., Xu, T., Sui, Y., Han, X.: Local buckling-induced forming method to produce metal bellows. Chin. J. Mech. Eng. **36**, 16 (2023). https://doi.org/10.1186/s10033-023-00852-2
5. Zhou, H., Yi, B., Wang, J., Zheng, X.: Preliminary investigation on plate bending with multiple-line induction heating. J. Marine Sci. Technol. (Japan) **25**, 455–466 (2020). https://doi.org/10.1007/S00773-019-00653-0
6. Zhu, Y., Luo, Y.: Fully coupled magneto-thermo-structural analysis by morphing method and its application to induction heating process for plate bending. Int. J. Appl. Electromagnet Mech **56**, 573–583 (2018). https://doi.org/10.3233/JAE-170076
7. Filkin, V., Vetyukov, Y., Heinrich, B., Toth, F.: Modelling the post-buckling behaviour of steel sheets under induction heating. PAMM **23**, 202300151 (2023). https://doi.org/10.1002/PAMM.202300151
8. Frogner, K., Andersson, M., Cedell, T., Siesing, L., Jeppsson, P., Ståhl, J.-E.: Industrial heating using energy efficient induction technology. In: 44th CIRP Conference on Manufacturing Systems, 2011 (2011)
9. Kadkhodaei, G., Sheshyekani, K., Hamzeh, M.: Coupled electric-magnetic-thermal-mechanical modelling of busbars under short-circuit conditions. IET Gener. Transm. Distrib. **10**, 955–963 (2016). https://doi.org/10.1049/IET-GTD.2015.0706
10. Takagaki, M., Toi, Y.: Coupled analysis of induction hardening considering induction heating, thermal elasto-viscoplastic damage, and phase transformation. Int. J. Damage Mech **19**, 321–338 (2009). https://doi.org/10.1177/1056789509103650
11. Nemkov, V.: Magnetic flux control in induction installations. In: Proceedings of the International Conference on Heating by Electromagnetic Sources, Padua, Italy, pp. 21–24 (2013)
12. Ida, N.: Engineering Electromagnetics, pp. 534–536. Springer, New York (2015). https://doi.org/10.1007/978-3-319-07806-9
13. Hanselman, D.C.: Brushless permanent-magnet motor design, pp. 21–24. McGraw-Hill, Inc., New York (1994)
14. Rudnev, V., Loveless, D., Cook, R.L., Black, M.: Handbook of Induction Heating. Manufacturing Engineering and Materials Processing, pp. 226–230. CRC Press, New York (2002)
15. Timoshenko, S.P., Gere, J.M.: Theory of Elastic Stability, 2nd edn., pp. 46–51. McGraw-Hill, Inc., New York (1963)
16. Emam, S., Lacarbonara, W.: A review on buckling and postbuckling of thin elastic beams. Eur. J. Mech. A. Solids **92**, 104449 (2022). https://doi.org/10.1016/J.EUROMECHSOL.2021.104449
17. Leipholz, H.: Über die Wahl der Ansatzfunktionen bei der Durchführung des Verfahrens von Galerkin. Acta Mech. **3**, 295–317 (1967). https://doi.org/10.1007/BF01179114
18. Liu, T., Li, Z.M., Qiao, P.: The closed-form solutions for buckling and postbuckling behaviour of anisotropic shear deformable laminated doubly-curved shells by matching method with the boundary layer of shell buckling. Acta Mech. **232**, 3277–3303 (2021). https://doi.org/10.1007/S00707-021-02952-3
19. Coman, C.D.: On the localised buckling of drillstrings in curved boreholes. Acta Mech. **235**, 369–390 (2024). https://doi.org/10.1007/S00707-023-03761-6
20. Verhulst, F.: The Poincaré-Lindstedt method, pp. 122–135. Springer, Berlin, Heidelberg (1996). https://doi.org/10.1007/978-3-642-61453-8_10
21. Vetyukov, Y.: Nonlinear Mechanics of Thin-Walled Structures: Asymptotics, Direct Approach and Numerical Analysis. Foundations of Engineering Mechanics, pp. 46–47. Springer, Vienna (2014)
22. Hale, J.K., Koçak, H.: Elementary Bifurcations, pp. 25–65. Springer, New York (1991). https://doi.org/10.1007/978-1-4612-4426-4_2